Highly reversible ambipolar photocurrents by modulating Ta in Ba2Bi2-xTaxO6 double perovskites

Guo, T.; Fu, W.T.; Groot, H.J.M. de

THE JOURNAL OF PHYSICAL CHEMISTRY C
A JOURNAL OF THE AMERICAN CHEMICAL SOCIETY

pubs.acs.org/JPCC
Article

Highly Reversible Ambipolar Photocurrents by Modulating Ta in $Ba_2Bi_{2-x}Ta_xO_6$ Double Perovskites

Tirong Guo, Wen Tian Fu, and Huub J. M. de Groot*

Cite This: J. Phys. Chem. C 2024, 128, 13177−13189
Read Online

ACCESS | Metrics & More | Article Recommendations | Supporting Information

ABSTRACT: Ta^{5+}-doped $Ba_2Bi_{2-x}Ta_xO_6$ ($0.2 \leq x \leq 0.8$) double perovskites are synthesized by a soft chemical sol−gel method. X-ray diffraction (XRD) results show the formation of a double perovskite structure. Systematic shifts of Bragg diffraction peaks to larger angles confirm the incorporation of increasing amounts of Ta^{5+} dopant ions in the $Ba_2Bi_2O_6$ (BBO) crystal lattice. The optical absorption spectra and Tauc plots reveal a monotonic increase of the optical band gaps for $Ba_2Bi_{2-x}Ta_xO_6$ ($0.2 \leq x \leq 0.8$) from 1.5 to 2.3 eV. Photoelectrochemical (PEC) and electrochemical tests signify the advantages of doping Ta^{5+} in improving the photoelectrode resistance to electrochemical corrosion. Highly reversible ambipolar photocurrents are observed for photoelectrodes with $x \geq 0.4$ that can be further enhanced by anodic or cathodic poling treatment for facilitated interface photocharge injection. $Ba_2Bi_{1.6}Ta_{0.4}O_6$ photoelectrodes exhibit both the highest cathodic photocurrent of 65.5 $\mu A\ cm^{-2}$ at 0 V_{RHE} with an onset potential of 1.43 V_{RHE}, and the highest anodic photocurrent of 37 $\mu A\ cm^{-2}$ at 2 V_{RHE} with an onset potential of 1.03 V_{RHE} among other Ta^{5+} containing counterpart samples. The deteriorating PEC photocurrents of photoelectrodes with $x \geq 0.5$ are the result of both inferior light absorption ability due to large band gaps and lower charge carrier concentrations due to defect compensation. The understanding and control of this switchable-photocurrent phenomenon by doping strategies are significant to further tailor the electronic band structure for compatible homojunctions of BBO-based double perovskites.

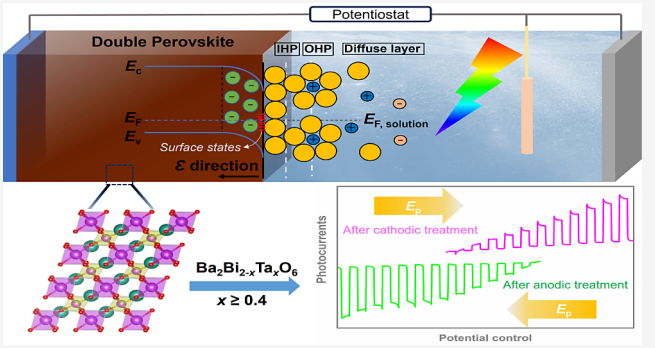

1. INTRODUCTION

Double perovskite semiconductor oxides $A_2B_2O_6$ are a family of potentially attractive materials with compositional flexibility from A-site or B-site cation modulation, precise control of the optical light absorption capability, and the electronic structure for solar energy conversion applications.[1] The $Ba_2Bi_2O_6$ (BBO) double perovskite system has been intensively investigated as a functional visible light responsive catalytic material.[2−4] Compositional engineering by cation doping plays a significant role in the modification of the crystal structure, the electronic band structure, and the subsequent photocatalytic activity.[3,5,6] It is believed that the B-site cations in the BBO double perovskite predominantly determine the electronic band structure and the physical properties, while the A-site cations contribute electrons for attaining charge neutrality.[7,8] The B-site cations in the BBO double perovskite parent compound are a mixed valence of Bi^{3+} and Bi^{5+} in a 1:1 ratio due to charge disproportionation. The $[BiO_6]$ octahedra are in an expanded and compressed alternating arrangement that is the result of a commensurate charge density wave (CDW) distortion caused by O−Bi bond displacement.[9,10] The electronic band structure of BBO has been commonly known for a high valence band maximum (VBM), which is ascribed to the filled strong antibonding states between the interaction of the Bi^{3+} $6s^2$ lone pair electrons and the O 2p orbitals, and a low conduction band minimum (CBM), which is determined by the empty low energy Bi^{5+} 6s orbitals.[9,11,12] Recently, it was found that band gap modulation by transition metal Nb^{5+} ion doping in the B-sites slightly increases the electronic band gap compared to the undoped BBO.[8,12] Beneficial optical light absorption properties and enhanced material electrochemical stability make the Nb^{5+}-doped BBO an excellent candidate material for photoelectrochemical (PEC) water splitting devices.[8,12,13]

In contrast to the parallel work of doping with group 3 element La at B-sites,[14] Ta and Nb are both group 5 elements, with an identical number of valence electrons in the outer shell, and share similar chemical and physical properties.[15] Since Ta and Nb are on different rows, the $Ta^{5+}([Xe]4f^{14}5d^06s^0)$ ion has an inner electronic configuration that is similar to the

Received: February 28, 2024
Revised: June 28, 2024
Accepted: July 15, 2024
Published: July 26, 2024

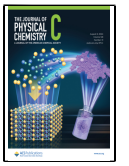

Bi^{5+}([Xe] $4f^{14}5d^{10}6s^{0}6p^{0}$) and is different from the Nb^{5+}([Kr]-$4d^{0}5s^{0}$) core electronic structure. In addition, the Ta^{5+} ionic radius with the coordination number of 6 for a [TaO_6] octahedron is 0.64 Å, which is close to the Bi^{5+} ionic radius in the [BiO_6] octahedron, 0.76 Å, indicating good compatibility for a stable Ta^{5+}-doped BBO double perovskite structure.[16] Earlier research has shown that the Ba_2BiTaO_6 (BBTO) double perovskite is a transparent p-type semiconductor material with a low valence band effective mass and a high hole mobility due to the spatially expanded Bi 6s-orbital hybridization with the O 2p-orbitals.[11] Attempts to decrease the optical band gap and enhance the transport properties of BBTO by K^+ doping improved the hole mobility from 21 cm^2 V^{-1} s^{-1} to 30 cm^2 V^{-1} s^{-1}. However, a negligible conductivity and a low charge carrier concentration on the order of around 10^{14} cm^{-3} hinder its application for efficient optoelectronics, either in the application of transparent electronics such as touch screens and thin film solar cells, or in the application of visible-light active hole transporting material for solar water splitting.[17,18] The cause of poor conductivity and low carrier concentration is deemed to be related to strong hole-killing defect charge compensation, i.e., oxygen vacancies and Ta on Bi antisites (Ta_{Bi}).[17,18]

It has been postulated that one beneficial way to mitigate the charge compensation effect in BBTO double perovskites for high charge carrier density is to increase the Bi content in the compound.[18] However, the Bi-rich compound BBO possesses a small optical band gap and an inefficient charge mobility.[11,17] Its inferior PEC water splitting performance correlates with the instability of the material surface.[12,19] Here in this work, a systematic study of the chemical composition of $Ba_2Bi_{2-x}Ta_xO_6$ (x = 0.2, 0.4, 0.5, 0.6, and 0.8) double perovskites is performed. Photoelectrodes are prepared to inspect and clarify the interrelationships between the modulation of the crystal structure of the material, the electronic band structure, and the behavior as a PEC photoelectrode for water oxidation or proton reduction in a laboratory setup, under calibrated 1 sun illumination. $Ba_2Bi_{2-x}Ta_xO_6$ (x = 0.2, 0.4, 0.5, 0.6, and 0.8) all crystallize in a double perovskite structure. Smaller grain sizes are formed when doping more Ta^{5+} ions. The optical band gap increases from 1.5 to 2.3 eV as the Ta-doping content increases. The electrochemical instability of $Ba_2Bi_{1.8}Ta_{0.2}O_6$ photoelectrodes is a major issue, while highly reversible ambipolar photocurrents are observed for photoelectrodes with $x \geq 0.4$. This intriguing polarizable behavior could be ascribed to the space charge polarization caused by the accumulated charge carriers in the grain boundaries,[20,21] or stem from the orientational crystal domain and domain wall effects,[22] which could vastly expand its application, e.g., not only to the protection overlayer and the visible-light responsive hole transporting layer for a homojunction structure with the La^{3+}-doped BBO system for solar water splitting,[14] but also to fulfill a demand for photocurrent-switchable optoelectronic devices.[23,24]

2. METHODS

2.1. Precursor Solution Preparation. The cation molar ratios of starting reagents were calculated based on the double perovskite formula $Ba_2Bi_{2-x}Ta_xO_6$ (x = 0.2, 0.4, 0.5, 0.6, and 0.8). For materials synthesis, existing procedures were adapted[12] by using Schlenk techniques for making homogeneous precursor solutions. $Ba(CH_3COO)_2$ (ACS reagent grade, Supelco.), $Bi(CH_3COO)_3$ (≥99.99%, Sigma-Aldrich), $Ta(OC_2H_5)_5$ (99.98%, Sigma-Aldrich), glacial acetic acid (≥99.99%, Sigma-Aldrich), anhydrous 2-methoxyethanol (99.8%, Sigma-Aldrich), and acetylacetone (≥99.5%, Sigma-Aldrich) were used as received.

5 mmol $Ba(CH_3COO)_2$ and $(5-2.5x)$ mmol $Bi(CH_3COO)_3$ were kept in vacuum (10^{-3} mbar) in the Schlenk bottle for 10 min, followed by purging with dried N_2. Then 5 mL of glacial acetic acid and 5 mL of anhydrous 2-methoxyethanol were injected into the bottle with a syringe. A small amount, 1 mL, of acetylacetone was added to reduce the sensitivity of metal salts to hydrolysis due to its chelating function.[25] The mixture was stirred for 10 min at room temperature before elevating the temperature to 70 °C with consistent magnetic stirring for 1 h. When the mixed solution cooled down to room temperature, $(2.5x)$ mmol $Ta(OC_2H_5)_5$ was then added and the whole solution was stirred for 1h to generate the precursor solution.

2.2. Perovskite Photoelectrode Preparations. Fluorine-doped tin oxide (FTO) coated glass (Sigma-Aldrich, TEC 7) was used as the conductive substrate for the photoelectrodes. FTO slides were ultrasonically cleaned with acetone, 2-propanol, and ethanol for 15 min. Before spin coating, the FTO glasses were thoroughly rinsed with Milli-Q water and dried in compressed air. Spin coating of the precursor solution on the substrate was carried out in ambient air with a rotation rate of 3500 rpm for 30 s. The precursor sample slides were then transferred into a muffle furnace at 550 °C for 1 h and quenched in the air. The spin coating and annealing process were repeated 4 times, with the last round of sample slides cooled naturally in the furnace. To validate the improvement of electrochemical stability by incorporation of Ta^{5+} ions in the crystal lattice, the undoped BBO perovskite electrodes were fabricated in the same workflow for reference.

2.3. Material Characterization. The crystal structure and phase composition of samples were characterized by X-ray powder diffraction (XRD) (PANalytical SR 5161). The optical absorbance spectrum of the photoelectrode was measured with a UV−vis spectrometer (Agilent, Cary 60). Surface morphologies were characterized by scanning electron microscopy (SEM) (Apreo). The photoelectrochemical performance was tested using an electrochemical potentiostat (Metrohm, Autolab/PGSTAT 128N) connected to a standard three-electrode cell with a quartz window under the illumination of an AM 1.5G solar simulator (Enlitech, SS-F5−3A) equipped with a 300 W Xe lamp (Enlitech, VE1558). An Ag/AgCl (1 M KCl) electrode and a Pt spiral wire were employed as the reference electrode and counter electrode, respectively. A buffer solution containing 0.1 M Na_2HPO_4 and 0.1 M NaH_2PO_4 was used as the testing electrolyte (pH ≈ 6.75) (Consort P901). The illumination intensity of the solar simulator was calibrated to 100 mW cm^{-2} by using a standard solar cell (Enli/SRC2020, SRC-00149) and a Keithley 2400 source meter. All PEC measurements of the sample electrodes were performed in a front-illumination configuration with a fixed working-electrode geometric surface area of 0.7854 cm^{-2}. The scan rate for linear sweep voltammetry (LSV) was kept constant at 10 mV s^{-1} with irradiation periods of 12 s (6 s on and 6 s off). The scan rate for cyclic voltammetry (CV) measurements was 50 mV s^{-1}. Electrochemical impedance spectroscopy (EIS) measurements were performed via the embedded FRA 32 M module (Metrohm, Autolab/PGSTAT 128N) using a 4-electrode measuring cell. The potentiostat signals at high frequencies (>10 kHz) were stabilized by

https://doi.org/10.1021/acs.jpcc.4c01309
J. Phys. Chem. C 2024, 128, 13177−13189

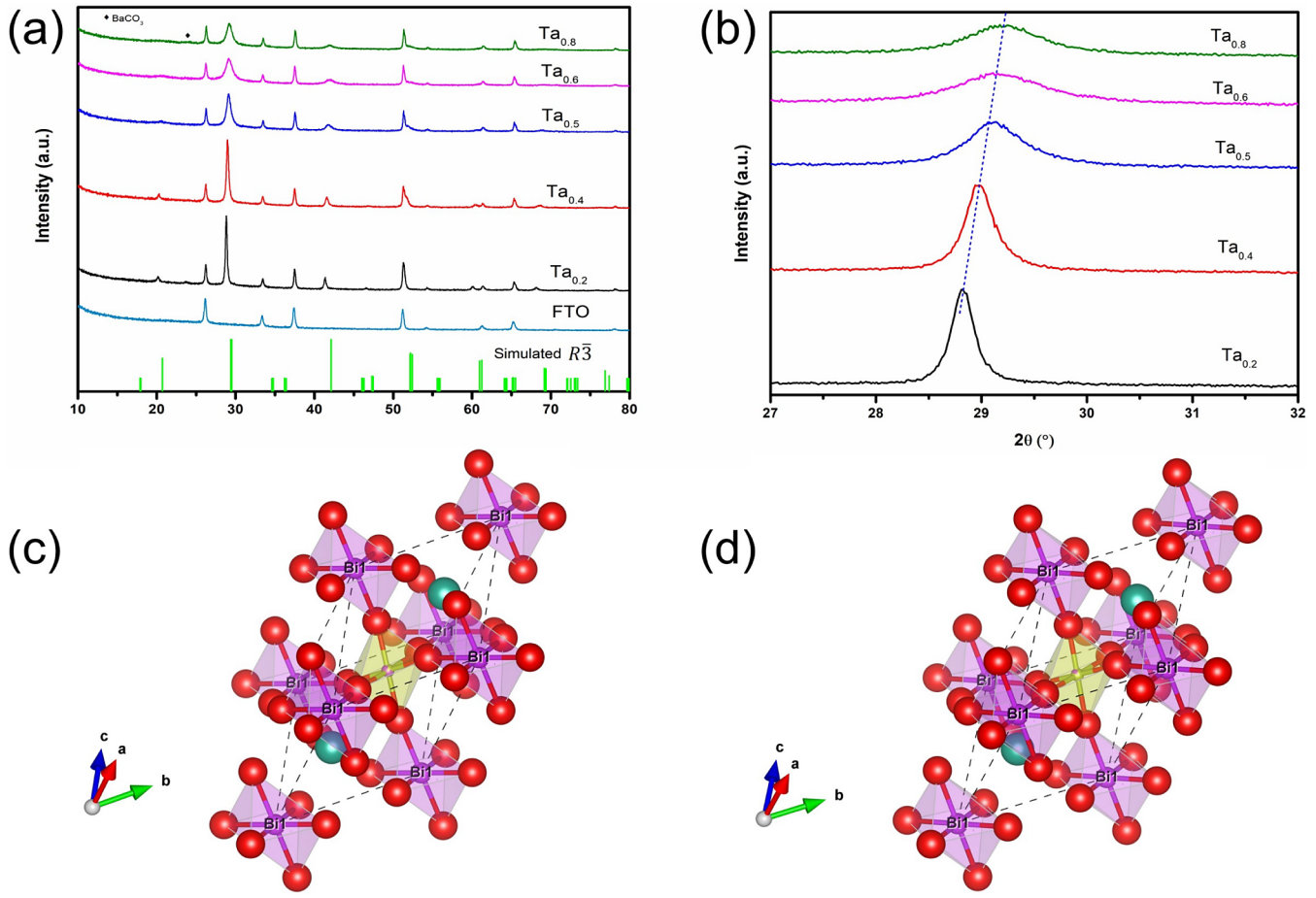

Figure 1. (a) XRD patterns of Ta-incorporated $Ba_2Bi_{2-x}Ta_xO_6$ ($0.2 \le x \le 0.8$) double perovskite series photoelectrodes with simulated reflections of BBTO in space group $R\bar{3}$[22] indicated in green bars and (b) detailed enlargement XRD patterns; schematic unit cell structures of (c) $Ba_2Bi_{1.8}Ta_{0.2}O_6$ and (d) $Ba_2Bi_{1.2}Ta_{0.8}O_6$, where green balls represent A-site Ba^{2+} ions, purple balls in purple octahedrons represent B1-site Bi^{3+} ions, purple balls in yellow octahedrons represent shared B2-site Bi^{5+} ions, yellow balls represent shared B2-site Ta^{5+} ions, and red balls represent O^{2-} ions.

connecting a 1 μF capacitor and a second Pt wire.[26] EIS data were recorded over a frequency range from 0.1 Hz to 100 kHz with an amplitude of 10 mV under open circuit potential (OCP) condition. Mott−Schottky (M−S) spectra were obtained in the reverse biased potential window of −0.225 V_{RHE} to 0.3 V_{RHE} in the dark with an amplitude of 10 mV and a frequency of 3 kHz. The scan measurements started from potentials more cathodic than the OCP, and scanning was ended several hundred millivolts before approaching OCP.[12] Potential scales versus Ag/AgCl ($V_{Ag/AgCl}$) were converted to potential scales versus the reversible hydrogen electrode (V_{RHE}) via the Nernst equation $V_{RHE} = V_{Ag/AgCl} + 0.059*pH + 0.23$.

3. RESULTS AND DISCUSSION

3.1. Crystal Structure and Film Morphologies. The crystal structures of photoelectrode samples with varying Ta-incorporation concentrations were characterized by X-ray powder diffraction. Diffraction from the bare substrate FTO was also measured as the background reference. All thin film photoelectrodes $Ba_2Bi_{2-x}Ta_xO_6$ with Ta-incorporation concentration from $x = 0.2$ to $x = 0.8$, as shown in Figure 1a, exhibit the double perovskite structure. The room temperature crystal structure of BBTO, with B2-sites fully occupied by Ta^{5+}, has previously been resolved and confirmed by Wallwork et al.[27] and Zhou and Kennedy.[22] By controlling the dopant concentration of Ta^{5+} ions in $Ba_2Bi_{2-x}Ta_xO_6$, a systematic and slight shift in diffraction peaks to lower angles is observed from sample $x = 0.8$ to $x = 0.2$. This shift correlates with the monotonic increase in the average B-site cation radii, from 0.847 Å for $x = 0.8$ to 0.883 Å for $x = 0.2$ as listed in Table S1, and is clearly illustrated in Figure 1. The parental BBTO adopts rhombohedral symmetry in the space group $R\bar{3}$,[22,27] as indicated by the green bars in Figure 1a. A recent report has further verified that the double perovskite $Ba_2Bi_{1.4}Ta_{0.6}O_6$, with B2-sites partially occupied by Ta^{5+}, also adopts the same space group $R\bar{3}$.[28] However, the space group change from monoclinic of BBO to rhombohedral of BBTO is outside the scope of the current investigation. The well-defined characteristic peaks of the $Ba_2Bi_{2-x}Ta_xO_6$ ($0.2 \le x \le 0.8$) in Figure 1a at around 20.7°, 29.3°, and 42.1° match well with the allowed $R\bar{3}$ reflections shown at the bottom. A minor secondary phase of $BaCO_3$ was detected for the $Ba_2Bi_{1.2}Ta_{0.8}O_6$ sample, indicating that pure single phases of high Ta-doping content samples are difficult to obtain when the sample is exposed to air during preparation.[29,30] Systematic perovskite tolerance factor calculations based on the equation $t = \frac{(r_A + r_O)}{\sqrt{2}(r_B + r_O)}$ are carried out, where r_A is the ionic radius of the A site cation, r_B is the average ionic radius of B site cations, and r_O is the ionic radius

https://doi.org/10.1021/acs.jpcc.4c01309
J. Phys. Chem. C 2024, 128, 13177−13189

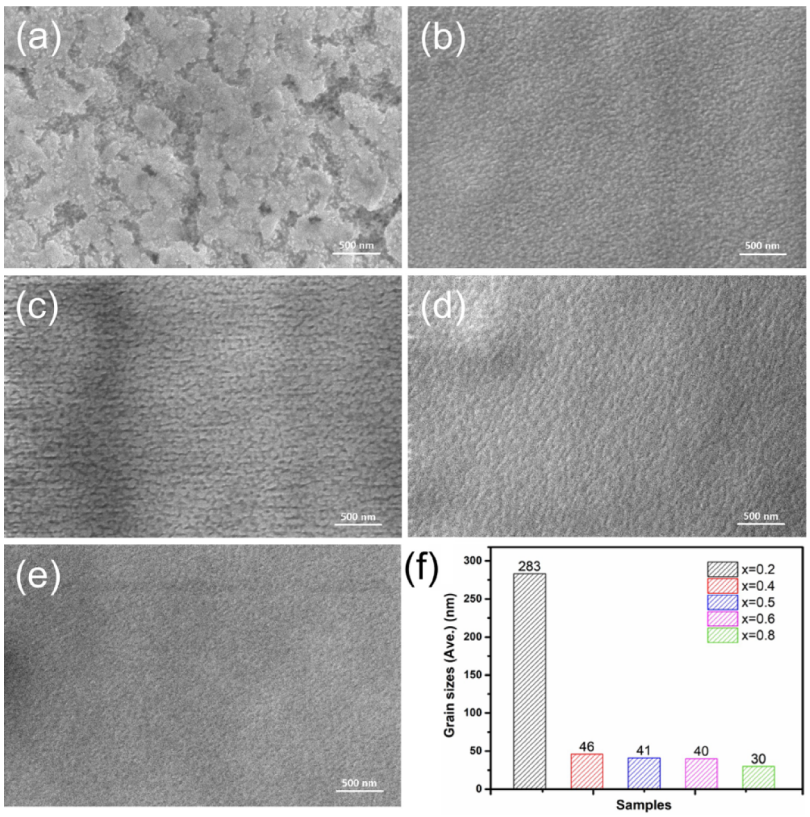

Figure 2. SEM surface morphologies of $Ba_2Bi_{2-x}Ta_xO_6$ ($0.2 \leq x \leq 0.8$) double perovskite thin films for (a) $x = 0.2$, (b) $x = 0.4$, (c) $x = 0.5$, (d) $x = 0.6$, (e) $x = 0.8$, and (f) average grain sizes.

of the O^{2-} anion. The calculated t values display a monotonous increase in a range from 0.932 to 0.947 for double perovskite samples $Ba_2Bi_{2-x}Ta_xO_6$ ($0.2 \leq x \leq 0.8$) from $x = 0.2$ to $x = 0.8$. The octahedral factors $\mu = r_B/r_O$ show a decreasing trend with the increase of Ta concentration resulting in a range of $0.631 > \mu > 0.605$. Tolerance factor and octahedral factor calculation results are listed in Table S1. From the perspective of perovskite design rules, the above calculated tolerance factors t and octahedral factors μ all allow the formation of stable perovskite structures with small lattice distortions.[31,32]

From the detailed enlargement patterns in Figure 1b, it is obvious that a varying Ta-incorporation concentration in the crystal structure slightly shifts the double perovskite characteristic peaks. The strongest double perovskite characteristic peaks at $28.8° < 2\theta < 29.3°$ shift to higher diffraction angles with lower intensities as the Ta concentration is increased. This is because the B-site Bi^{5+} has a larger ionic radius of 0.76 Å compared to 0.64 Å for Ta^{5+}, which leads to smaller lattice parameters and interplanar crystal spacing when adding more Ta^{5+} dopant ions. The lattice microstrain fields surrounding the lattice dislocation defects accompanying the introduced Ta^{5+} could also possibly shift the Bragg diffraction peaks if the strain is uniform.[33] Hence, the characteristic shift of the main peaks is in accordance with the systematic changes in the crystal structure and demonstrates the successful intercalation of the Ta^{5+} ions. The unit cell evolution from $Ba_2Bi_{1.8}Ta_{0.2}O_6$ to $Ba_2Bi_{1.2}Ta_{0.8}O_6$ was illustrated in Figure 1c,d with the Bi^{5+} site occupancy changing from 0.8 to 0.2. In addition, the full width at half-maximum (FWHM) of the characteristic reflection peak adjacent to $2\theta \approx 29°$ increases for increasing Ta concentration (Figure 1b). This could be the result of the formation of smaller crystalline domains based on the expression of the Scherrer equation $D = \frac{K\lambda}{B \cos \theta}$, where D is the ordered crystallite size perpendicular to the lattice planes under diffraction analysis, K is the Scherrer constant, $\lambda = 1.54$ Å is the wavelength of the X-ray beam used, B is the FWHM of the peak in radians, and θ is the Bragg angle.[34] The diffraction peak broadening was also reported to be related to domain wall effects in the high Ta content sample of BBTO,[22] where crystal domains were separated by domain walls to accommodate local crystal strain when crystallites are formed. The gradual peak broadening with an increasing Ta concentration from 0.2 to 0.8 could also be partially related to this feature. In addition, the diffraction from double perovskites $Ba_2Bi_{2-x}Ta_xO_6$ ($0.2 \leq x \leq 0.8$) results in the characteristic peaks at around 51°−52°. The diffraction peak from sample $x = 0.2$ is adjacent to and overlaps with the FTO signal at $2\theta = 51°$. With the gradual increase in Ta^{5+} concentration, the double perovskite diffraction peaks gradually shift to higher angles, with larger differences from the FTO peak at $2\theta = 51°$ and forming visible shoulder signals in sample $x = 0.4$ and $x = 0.5$ in Figure 1a. However, the shoulder peaks for samples $x = 0.6$ and $x = 0.8$ appear to be increasingly flat due to the increasing peak broadening effects.

Surface structure and morphologies of double perovskite photoelectrodes $Ba_2Bi_{2-x}Ta_xO_6$ ($0.2 \leq x \leq 0.8$) were characterized by SEM images. As shown in Figure 2a, the photoelectrode $Ba_2Bi_{1.8}Ta_{0.2}O_6$ has a rough surface and is microstructured. Submicron grains with a size of around 283 nm are stacked together, and abundant voids are formed between the grains. In contrast, photoelectrodes $Ba_2Bi_{1.6}Ta_{0.4}O_6$, $Ba_2Bi_{1.5}Ta_{0.5}O_6$, $Ba_2Bi_{1.4}Ta_{0.6}O_6$, and

https://doi.org/10.1021/acs.jpcc.4c01309
J. Phys. Chem. C 2024, 128, 13177−13189

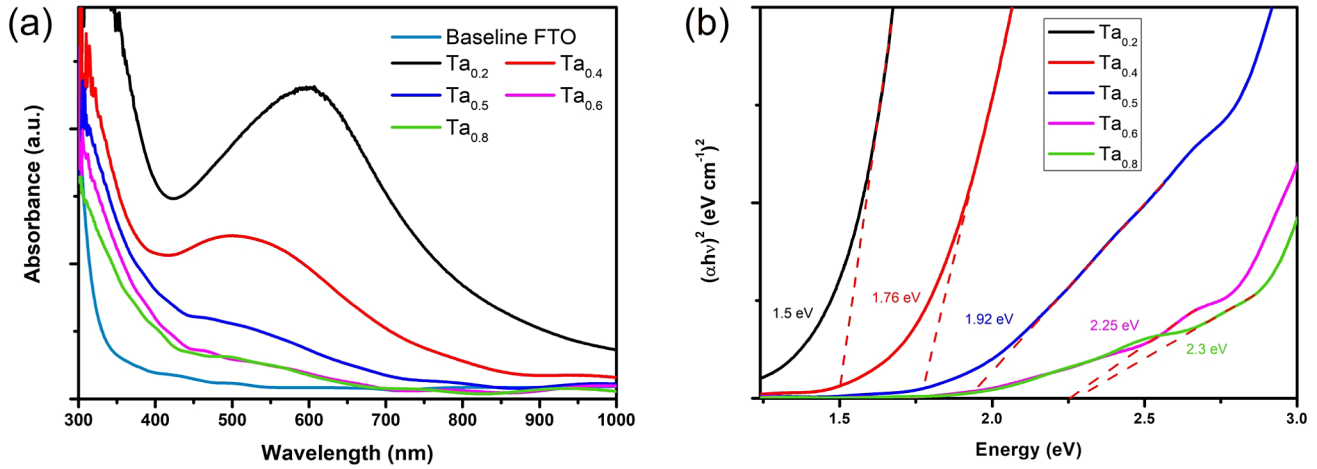

Figure 3. (a) Optical absorption and (b) direct Tauc-plot of Ta-incorporated $Ba_2Bi_{2-x}Ta_xO_6$ ($0.2 \leq x \leq 0.8$) double perovskite thin films grown on the FTO substrate.

$Ba_2Bi_{1.2}Ta_{0.8}O_6$ in Figure 2b–e all show a uniform close-packed morphology. To validate the small grain sizes, SEM images collected at a high resolution are displayed in Figure S1. The statistical averages of the component grain sizes reveal a decreasing trend, from 46 to 30 nm, when increasing the Ta concentration from 0.4 to 0.8 (Figure 2f). The decrease in apparent grain size with raising Ta concentration is in line with the observed XRD peak broadening in Figure 1b.

3.2. Optical Absorption Properties of Film Photoelectrodes. The optical properties of $Ba_2Bi_{2-x}Ta_xO_6$ ($0.2 \leq x \leq 0.8$) double perovskite series photoelectrodes are shown in Figure 3a. All sample photoelectrode absorbance data are represented after FTO baseline subtraction. Among the photoelectrodes, $Ba_2Bi_{1.8}Ta_{0.2}O_6$ exhibits the broadest absorption spectrum, with an absorption maximum in the visible light range at around 600 nm and a cutoff wavelength at around 830 nm. Sample photoelectrodes $Ba_2Bi_{1.6}Ta_{0.4}O_6$ and $Ba_2Bi_{1.5}Ta_{0.5}O_6$ also both show a broad absorption peak in the visible light range, with absorption cutoff wavelengths of 700 and 650 nm, respectively. In contrast, when increasing the Ta content to 0.6 or 0.8, the absorption in the visible light region sharply decreases to very low levels. This observation is in line with the variation in sample colors, as shown in Figure S2a. Sample $Ba_2Bi_{1.8}Ta_{0.2}O_6$ and $Ba_2Bi_{1.6}Ta_{0.4}O_6$ are almost black, $Ba_2Bi_{1.5}Ta_{0.5}O_6$ is dark brown, while $Ba_2Bi_{1.4}Ta_{0.6}O_6$ and $Ba_2Bi_{1.2}Ta_{0.8}O_6$ are light brown. The ability to absorb light and the optical color change with increasing Ta concentration in the sample series correlate with changes in the electronic band structures. As has been calculated from the Tauc-plot in Figure 3b, the optical band gaps for $Ba_2Bi_{2-x}Ta_xO_6$ ($0.2 \leq x \leq 0.8$) photoelectrodes show values of 1.5 eV, 1.76 eV, 1.92 eV, 2.25 eV, and 2.3 eV for sample series from low Ta concentration $Ba_2Bi_{1.8}Ta_{0.2}O_6$ to high Ta concentration $Ba_2Bi_{1.2}Ta_{0.8}O_6$.

For further comparison, the optical property of the undoped BBO is depicted in Figure S2b, where a large visible light absorption peak centered at around 650 nm with the absorption edge at around 850 nm shows up, indicating an optical band gap of 1.48 eV. In addition, the high Ta content material $Ba_2Bi_{1.125}Ta_{0.875}O_6$ and the transparent semiconductor BBTO were both reported with wider band gaps of 2.56 eV[18] and 3.2 eV,[11] respectively, than the obtained 2.3 eV for the above as-prepared $Ba_2Bi_{1.2}Ta_{0.8}O_6$. The experimental optical band gaps are monotonically raising from 1.5 to 2.3 eV for the sample series $Ba_2Bi_{2-x}Ta_xO_6$ ($0.2 \leq x \leq 0.8$) and are well within the band gap limits of the earlier reports.[11,18] The correlation between the Ta incorporation concentration in BBO-based double perovskites and the optical properties could be explained by the systematic changes in the electronic band structures. The electronic structure has been considered to be related to the interaction between B-site Bi electronic states and O 2p states, while the A-site Ba showed negligible electronic effect, confirming the inactive nature of this site.[10] Ordered B-site local charge disproportionation of Bi^{3+} and Bi^{5+} and the oxygen breathing mode for the Bi–O CDW distortions in the crystal lattice leads to band splitting in the electronic structure involving the Bi^{3+} $6s^2$ states, the Bi^{5+} $6s^0$ states, and the O 2p states and thus the formation of two subbands in the pure compound BBO.[9,35] The filled antibonding states that are the result of strong hybridization interaction between Bi^{3+} $6s^2$ lone pair states and O 2p states form the VBM, while the unoccupied Bi^{5+} 6s orbitals form the CBM.[9,11,36] With the substitution of Ta^{5+} ions for constituent Bi^{5+} ions in the lattice, Ta^{5+} 5d empty orbitals with high energy contribute to the conduction band (CB) and diminish the contribution from the low energy Bi^{5+} 6s empty orbitals, thus lifting the CBM to higher energy levels and enlarging the bandgap. In this regard, modulation of the electronic band structure by increasing the Ta-incorporation concentration in BBO would progressively increase the band gaps to large values, which is well in line with the experimental results in Figure 3.

3.3. PEC Properties of Film Photoelectrodes. Photoelectrochemical and electrochemical experiments were carried out to analyze the PEC performance of the as-prepared series of photoelectrodes. The low Ta-incorporation concentration $Ba_2Bi_{1.8}Ta_{0.2}O_6$ photoelectrode undergoes electrochemical corrosion, which can be partially suppressed by adding more Ta. In Figure S3a, only negligible photon-responsive current is obtained at the potential range from 0.8 to 1.3 V_{RHE} for low Ta incorporation $Ba_2Bi_{1.8}Ta_{0.2}O_6$. A giant electrochemical reduction peak centered at around 0.5 V_{RHE} and the following steep polarization reduction slope at lower potentials could be ascribed to reduction reactions of the Bi ions present in the system. As has been further confirmed by the electrochemical cyclic voltammetry (CV) patterns of the undoped BBO photoelectrode in the dark, the first CV scan depicted detailed

https://doi.org/10.1021/acs.jpcc.4c01309
J. Phys. Chem. C 2024, 128, 13177−13189

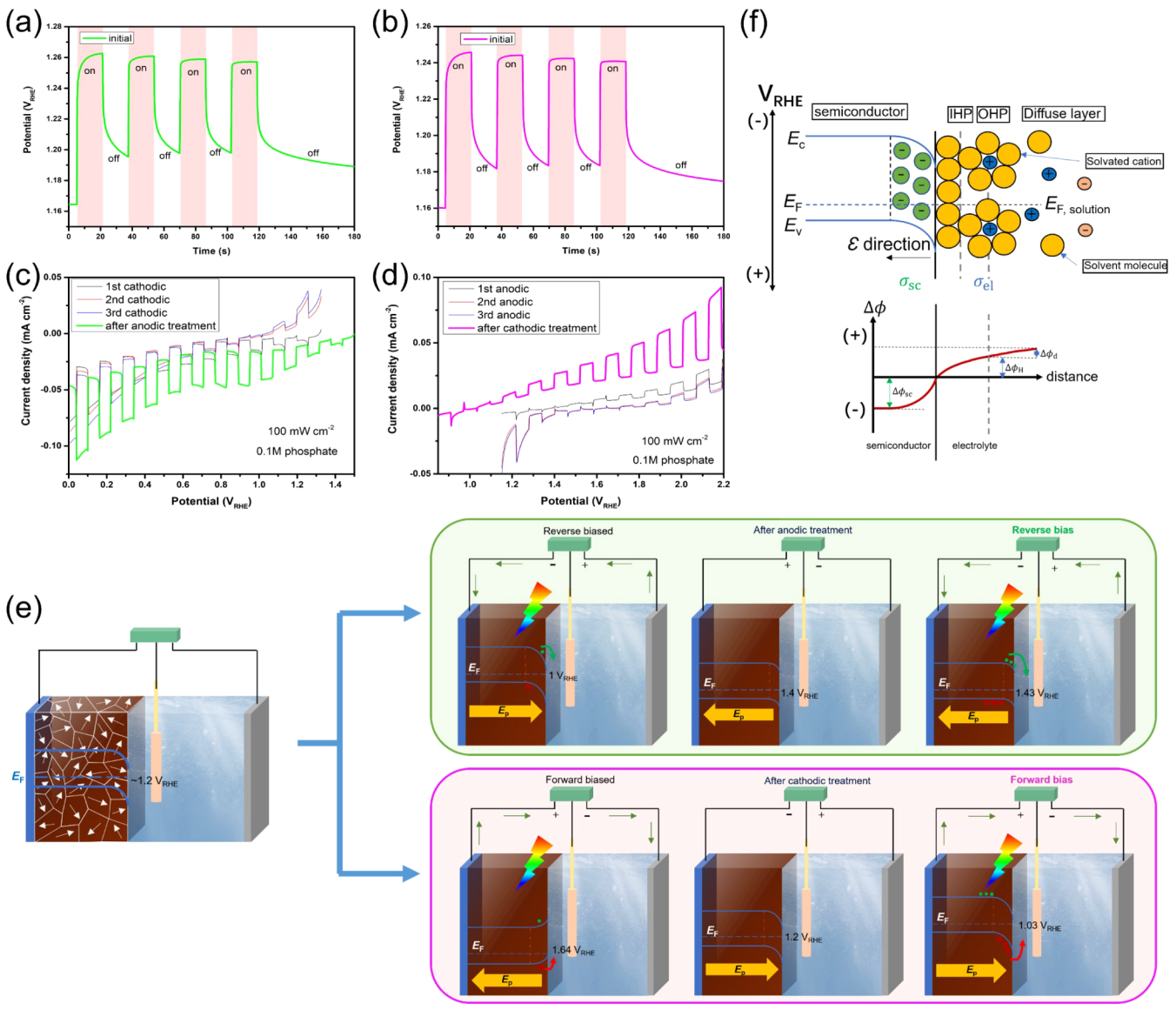

Figure 4. PEC measurements of $Ba_2Bi_{1.6}Ta_{0.4}O_6$ photoelectrodes in 0.1 M sodium phosphate electrolyte (pH ≈ 6.75): (a) OCP pattern before reverse bias and (c) LSV curves with reverse bias under intermittent illumination; (b) OCP pattern before forward bias and (d) LSV curves with forward bias under intermittent AM 1.5G illumination; (e) energy diagrams under reverse potential scan scheme with anodic treatment (in the upper green frame) and under forward potential scan with cathodic treatment (in the lower magenta frame); E_p: induced polarization field; electrons are represented in green solid balls and holes are represented in red hollow balls; (f) a simplified p-type photoelectrode/electrolyte interface structure in thermal equilibrium in dark condition (upper panel) and the corresponding potential profile (lower panel) given with respect to the flat band situation; $\boldsymbol{\varepsilon}$: built-in electric field vector near the semiconductor surface, IHP: inner Helmholtz plane, OHP: outer Helmholtz plane, σ_{sc}: net excess charge in the photoelectrode space charge region; σ_{el}: net excess charge in the electrolyte; $\Delta\phi$: electrostatic inner potential scale change of a condensed phase (the semiconductor or the electrolyte); E_c: conduction band energy; E_v: valence band energy; E_F: Fermi level energy.

reduction information in Figure S3b. Besides the main reduction peak at 0.5 V_{RHE}, a reduction shoulder at around 0.75 V_{RHE} and a small reduction peak at around 1.2 V_{RHE} occur first. This broad cathodic peak at around 1.2 V_{RHE} could be attributed to a thermodynamically facile reduction of Bi^{5+} to Bi^{4+} ($E^0_{Bi^{5+}/Bi^{4+}}$=2 V_{SHE}). The subsequent reduction shoulder at 0.75 V_{RHE} and the main reduction peak at 0.5 V_{RHE} could be related to the reduction of Bi^{4+} to Bi^{3+} ($E^0_{Bi^{4+}/Bi^{3+}}$=1.59 V_{SHE}) and possibly a combination process involving two electrons overall Bi^{5+} to Bi^{3+} ($E^0_{Bi^{5+}/Bi^{3+}}$=1.8 V_{SHE}) conversion, as indicated by the large reduction peak area for a large amount of charges transferred.[37] The steep reduction slope at around 0.2 V_{RHE} to increasingly cathodic potentials in both Figure S3ab could be due to further complex reduction reactions of Bi^{3+} species.

Vivier and coworkers have discussed the Bi^{3+} electrochemical reduction mechanisms.[38] The reduction mechanisms first involved an adsorption process where adsorbed ionic Bi^{3+} species were reduced into $Bi^{(0)}$ ($E^0_{Bi^{3+}/Bi^{(0)}}$=0.3 V_{SHE}) and would cause a weak cathodic signal. The main cathodic processes were based on the stepwise reduction of solvated Bi^{3+} ions into Bi^{+} ($E^0_{Bi^{3+}/Bi^{+}}$=0.2 V_{SHE}) and concomitant $Bi^{(0)}$, which resulted in the strong cathodic signal observed at around 0.2 V_{RHE} to lower potentials.[37,38] These two reduction processes were further confirmed by the occurrence of two oxidation peaks at around 0.4 V_{RHE} and 0.6 V_{RHE} in the reverse oxidation scan,[38]

https://doi.org/10.1021/acs.jpcc.4c01309
J. Phys. Chem. C 2024, 128, 13177−13189

which are highly consistent with the two reoxidation processes in Figure S3b. In contrast to the undesirable characteristics of Bi-rich compounds prone to electrochemical reduction, incorporating Ta ions in the lattice is hypothesized to be beneficial for improving the stability of the material since the redox potentials of Ta-containing species are lower than Bi-containing species.[37] The strong electrochemical parasitic corrosion reactions for undoped BBO and low Ta-incorporated $Ba_2Bi_{1.8}Ta_{0.2}O_6$ photoelectrodes indicate the necessity for further increasing Ta concentration than $x = 0.2$ in the BBO-based double perovskite compounds.

PEC performances of $Ba_2Bi_{1.6}Ta_{0.4}O_6$ photoelectrodes in neutral electrolyte are shown in Figure 4. The dark OCP values of $Ba_2Bi_{1.6}Ta_{0.4}O_6$ photoelectrodes are around 1.16 V_{RHE} and are the result of thermal equilibrium for electron transfer between the semiconductor photoelectrode Fermi level, E_F, and the redox electron energy level, $E_{F,solution}$, from the contacting electrolyte side at the semiconductor/electrolyte interface.[39] The E_F of the semiconductor photoelectrode can also be affected by nonideal electrode factors such as surface states in the thermal equilibrium process.[40] The OCP in an electrochemical cell is a good approximation of the potential difference between the E_F of the majority charge carriers in the semiconductor photoelectrode and the potential of the reference electrode (RE).[41] A change in OCP, ΔOCP, from its initial value in the dark to the OCP under light illumination, reflects the energy level change of the semiconductor E_F. Strong light responses of ΔOCP around 65 mV under intermittent 100 mW cm^{-2} illumination are observed for the $Ba_2Bi_{1.6}Ta_{0.4}O_6$ photoelectrode in Figure 4a,b. The positive shift of the OCP under illumination is in good agreement with the p-type conductivity.[11,12] As illustrated in Figure 4f, at equilibrium excess negative charges σ_{sc} residing in the semiconductor space charge region (SCR) leads to a built-in electric field $\boldsymbol{\varepsilon}$ pointing toward the semiconductor bulk, and the semiconductor surface energy bands bend down toward the electrolyte. The expression of E_F for the majority charges (h^+) of a p-type semiconductor photoelectrode is presented in the Supporting Information. As a result of the spatial distribution of excess charges σ_{sc} and σ_{el}, the potential drop $\Delta\phi$ across the electrode/electrolyte interface would start from a negative potential, whose magnitude would decrease to zero at the interface with a potential offset $\Delta\phi_{sc}$. On the electrolyte side, the $\Delta\phi_{el}$ changes the sign and increase the potential from the interface double layer area by a potential drop of $\Delta\phi_H$ to a steady value in the bulk electrolyte by a potential drop of $\Delta\phi_d$, respectively,[42] as shown in Figure 4f. When applying 100 mW cm^{-2} irradiation on this junction, photon excited e^- and h^+ pairs in the semiconductor are separated in opposite directions by the ε in the SCR. The e^- are driven to the semiconductor/electrolyte interface, while the h^+ are driven to the bulk of the semiconductor. A new steady equilibrium at this junction under 1 sun's illumination subsequently forms, after the rearrangement of net excess charges in the semiconductor and the electrolyte phase. The original negative excess charges σ_{sc} in the dark are partially canceled out and both the built-in $\boldsymbol{\varepsilon}$ and the amount of band bending $\Delta\phi_{sc}$. are decreased. As a result, the potential profile $\Delta\phi$ across the electrode/electrolyte interface becomes more gradual and tends to be flattened under illumination due to a major removal of negative σ_{sc} in the SCR. The position of the semiconductor electrode E_F, therefore, shifts down to a more negative energy level with respect to the RE, which is consistent with the notable anodic shift behavior upon illumination in the OCP values in Figure 4a,b. A description for the equations is summarized in the Supporting Information. If the irradiation is intensive and the illumination on the photoelectrode is saturated, $\Delta\phi_{sc}$ could further be reduced to zero and the whole semiconductor interior becomes field free, $\boldsymbol{\varepsilon} = 0$ and $\sigma_{sc} = 0$, without surface band bending. Most probably 1 sun is insufficient to saturate the light-induced OCP,[43,44] and hence the field-free flat band potential of the $Ba_2Bi_{1.6}Ta_{0.4}O_6$ photoelectrode is more positive than 1.26 V_{RHE} (Figure 4a,b). When the illumination is removed, the dark OCPs consistently show cathodic shifts to around 1.2 V_{RHE}, which is slightly more positive of the dark OCP value around 1.16 V_{RHE} at the start of the experiment. This phenomenon could be ascribed to the trapping of photogenerated h^+ in the surface states of the photoelectrode. As the excess charges from the trapped h^+ on the photoelectrode surface would change the ionic charge distribution in the electrolyte, inducing additional negative charge in the diffuse layer and an overall decreased net positive σ_{el} density, the $\Delta\phi$ thus becomes less precipitous comparing to the situation without charged species residing on the photoelectrode surface (Figure 4f). In parallel, a compromise in the net negative σ_{sc} by the surface h^+ trapping would lead to a reduced magnitude of the photoelectrode $\Delta\phi_{sc}$ and sightly shift down the E_F to a more negative value, which correlates to an increased energy difference and a more positive electric potential value versus the RE.[39,45]

The LSV performances of $Ba_2Bi_{1.6}Ta_{0.4}O_6$ photoelectrodes are shown in Figure 4c,d. Apparently, the electrochemical stability of the $Ba_2Bi_{1.6}Ta_{0.4}O_6$ photoelectrode has been greatly enhanced compared to those of the undoped BBO photoelectrode and the $Ba_2Bi_{1.8}Ta_{0.2}O_6$ photoelectrode by incorporating more Ta ions in the double perovskite framework. In the cathodic scan scheme (Figure 4c), the photocurrent onset potential starts at around 1.2 V_{RHE} in the first round scan, which is consistent with the corresponding stabilized dark-field OCP values. In the following two consecutive cathodic LSV scans, the cathodic photocurrent onset potentials shift to more cathodic values at around 1 V_{RHE} and the opposite anodic photocurrents appear at potentials higher than 1 V_{RHE}. The detection of anodic photocurrents indicates the injection of photogenerated h^+ from the semiconductor photoelectrode toward the electrolyte, while the subsequent cathodic photocurrents in the same scan at lower applied potentials dominate the trace both due to the increasing preferential build-in ε in the SCR and the elevated high energy photogenerated e^- transfer at the interface. The cathodic LSV pattern after the anodic polarization treatment shows significant improvement with the onset potential shifting to around 1.43 V_{RHE} and a difference of 65.5 μA cm^{-2} at 0 V_{RHE} between the photocurrent density and the dark current density. The obvious cathodic photocurrent increase at a higher potential range after anodic treatment demonstrates better e^-—h^+ pairs separation and more efficient e^- injection at the photoelectrode/electrolyte junction.

When further investigating the anodic LSV behavior of the $Ba_2Bi_{1.6}Ta_{0.4}O_6$ photoelectrode (Figure 4d), a small cathodic photocurrent is observed in the potential range of 1.2 V_{RHE} to 1.4 V_{RHE} in the first scan, indicating that e^- in the photoelectrode SCR are separated and driven to the electrolyte side for the reduction reaction. Photocurrent reversion at around 1.4 V_{RHE} to more positive potentials manifested the reversed direction of photogenerated charge transfer at the

https://doi.org/10.1021/acs.jpcc.4c01309
J. Phys. Chem. C 2024, 128, 13177−13189

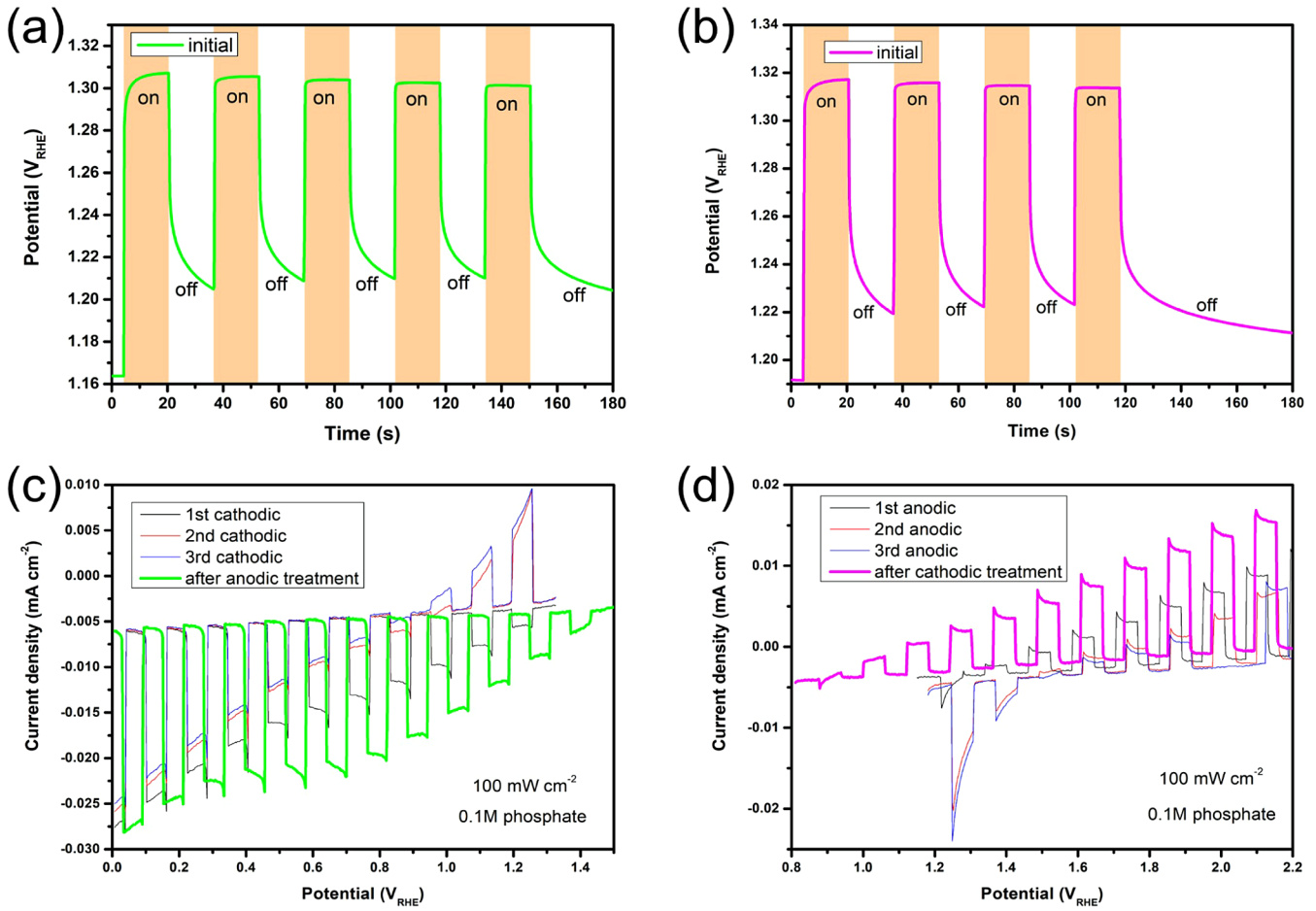

Figure 5. PEC measurements of $Ba_2Bi_{1.5}Ta_{0.5}O_6$ photoelectrodes in 0.1 M sodium phosphate electrolyte (pH ≈ 6.75): (a) OCP responses before reverse bias and (c) LSV curves with reverse bias under intermittent AM 1.5G illumination; (b) OCP responses before forward bias and (d) LSV curves with forward bias under intermittent illumination.

electrode/electrolyte junction, namely, the h^+ injection toward the electrolyte. In the following 2 anodic LSV scans, the cathodic photocurrent becomes more prominent at around 1.2 V_{RHE} and the anodic photocurrent onset shifts to a more positive value of around 1.64 V_{RHE}. After the cathodic polarization treatment, the anodic LSV scan with forward bias shows both a negative shift of the onset potential to around 1.03 V_{RHE} and substantial increases in the anodic photocurrent densities to 37 μA cm^{-2} at 2 V_{RHE}. In addition to the increase in the anodic photocurrent, the dark current also increases accordingly. This could be the result of photoelectrode energy level degeneracy under large forward bias, where the photoelectrode behaves resembling a metal electrode and oxidation reactions facilitated by the thermodynamic driving force in the dark condition would occur.[39] Similar experimental phenomena of such highly polarizable ambipolar photocurrents were also observed in other PEC systems,[23,24,46,47] where an internal polarization field modulated by the external poling bias accounts for the explanation. Earlier studies in the electronic dielectric properties and relaxation processes of BBTO double perovskite materials revealed contributions from crystal grains and grain boundaries.[29,30] The relaxation at high frequencies is assumed to be related to the highly conducting grains, while the relaxation at low frequencies is related to poorly conducting grain boundaries.[29] The electronic dielectric dependence of BBTO on frequency indicates that the dipoles of the material could follow the excitation at low frequency, and would lag behind the electric field at high frequency.[30] Recently, a report pointed out that the B-site induced lattice distortion in double perovskites could also influence the dielectric relaxation related to the accumulation of charge carriers in the grain boundaries.[20] Due to the high resistance of the grain boundaries, these accumulated charge carriers could lead to the space charge polarization.[21] The analogous orientational crystal domains and domain wall effects in BBTO materials brought up by Zhou and Kennedy could also be partly responsible for the observed polarizable properties of $Ba_2Bi_{1.6}Ta_{0.4}O_6$ photoelectrodes.[22]

The polarization diagram of the $Ba_2Bi_{1.6}Ta_{0.4}O_6$ photoelectrode during LSV scans is schematically illustrated in Figure 4e. Under reverse scan in the cathodic direction, a polarization internal electric field E_p builds up by orienting the miscellaneous dipole directions pointing toward the electrolyte as shown in the upper green panel, while the preexisting electric field ε in the semiconductor SCR is pointing inward into the bulk of the semiconductor. As a result, in the second and third cathodic scan, the polarization field E_p could drive h^+ injection into the electrolyte phase at potentials higher than 1 V_{RHE}, at which the $\boldsymbol{\varepsilon}$ could be smaller than E_p. As the $\boldsymbol{\varepsilon}$ is becoming larger at potentials lower than 1 V_{RHE}, the overall electric field is dominated by the interfacial $\boldsymbol{\varepsilon}$, with e^- transfer

https://doi.org/10.1021/acs.jpcc.4c01309
J. Phys. Chem. C 2024, 128, 13177−13189

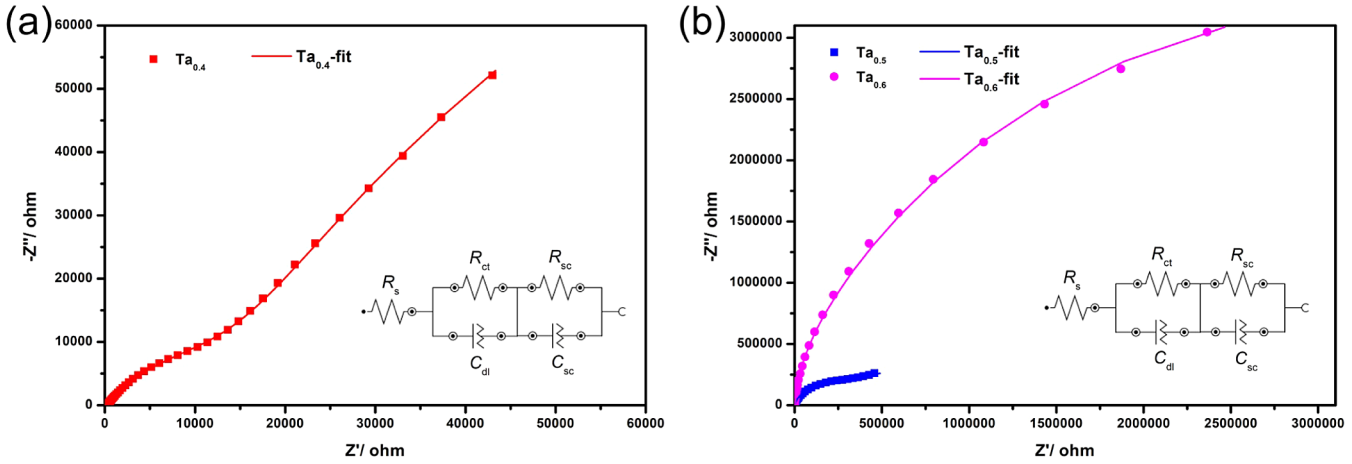

Figure 6. Nyquist plots of photoelectrodes (a) $Ba_2Bi_{1.6}Ta_{0.4}O_6$, (b) $Ba_2Bi_{1.5}Ta_{0.5}O_6$ and $Ba_2Bi_{1.4}Ta_{0.6}O_6$ in the dark at the OCP condition in the neutral 0.1 M sodium phosphate buffer solution. The EIS data are fitted and simulated according to the inserted equivalent circuit model.

Table 1. Simulated Parameters of the Equivalent Circuit Elements from the EIS Data of Thin Film Photoelectrodes $Ba_2Bi_{1.6}Ta_{0.4}O_6$, $Ba_2Bi_{1.5}Ta_{0.5}O_6$, and $Ba_2Bi_{1.4}Ta_{0.6}O_6$

	R_s/Ω	R_{ct}/Ω	C_{dl}/F	R_{sc}/Ω	C_{sc}/F
$Ta_{0.4}$	296.56	3.38×10^5	5.10×10^{-6}	1.36×10^4	2.68×10^{-6}
$Ta_{0.5}$	296.00	5.33×10^5	1.83×10^{-6}	2.77×10^5	4.94×10^{-7}
$Ta_{0.6}$	295.20	6.76×10^6	2.79×10^{-7}	4.10×10^5	8.27×10^{-7}

toward the electrolyte for the cathodic photocurrent. After the anodic polarization treatment, the polarization field E_p could be flipped pointing toward the semiconductor bulk. The overall electric field is enhanced since the directions of E_p and $\boldsymbol{\varepsilon}$ are aligned, which could well facilitate the separation of photogenerated e^-–h^+ pairs and drive e^- to the interface for interfacial reduction reactions as shown in Figure 4c,e upper panel. The polarization sequence is in the opposite situation under anodic forward LSV measurements. In the first anodic LSV scan for a fresh $Ba_2Bi_{1.6}Ta_{0.4}O_6$ photoelectrode, a tiny cathodic photocurrent is detected at around 1.2 V_{RHE}, indicating the e^- injection toward the electrolyte. In the second and the third anodic scan, the cathodic photocurrents at 1.2 V_{RHE} become more prominent and the anodic photocurrents that occurred at potentials higher than 1.64 V_{RHE} decrease under the influence of the polarization field E_p pointing inward into the semiconductor bulk. After the cathodic polarization treatment, the E_p is reoriented to point toward the electrolyte, which could enhance the h^+ transfer to the photoelectrode/electrolyte interface and improve the anodic photocurrent as shown in Figure 4d,e lower panel.

In Figure 5a,b, the ΔOCP induced by intermittent 1 sun's irradiation is about 100 mV, which is indicative of larger degree of surface energy bands bending of $Ba_2Bi_{1.5}Ta_{0.5}O_6$ photoelectrode compared to the $Ba_2Bi_{1.6}Ta_{0.4}O_6$ photoelectrode. The polarization model discussed above is further verified by the well enhanced cathodic photocurrents after anodic polarization treatment and the elevated anodic photocurrents after cathodic polarization treatment, as shown both in Figure 5c,d and Figure S4. A minor constant dark current is observed within the potential range, which could be due to a slow decomposition of the photoelectrodes.[48] Alternatively, this potential-independent dark current could also be the result of thermal generation related to abundant surface states with electron tunneling at the surface.[49] In contrast to the $Ba_2Bi_{1.6}Ta_{0.4}O_6$ photoelectrode, the collected cathodic photocurrent densities at 0 V_{RHE} reach around 22.3 $\mu A\ cm^{-2}$ for the $Ba_2Bi_{1.5}Ta_{0.5}O_6$ photoelectrode and 8.8 $\mu A\ cm^{-2}$ for the $Ba_2Bi_{1.4}Ta_{0.6}O_6$ photoelectrode, respectively. The anodic photocurrent densities at 2 V_{RHE} deliver around 14.5 $\mu A\ cm^{-2}$ for the $Ba_2Bi_{1.5}Ta_{0.5}O_6$ photoelectrode and 7.6 $\mu A\ cm^{-2}$ for the $Ba_2Bi_{1.4}Ta_{0.6}O_6$ photoelectrode, respectively. The decreasing photocurrents for increasing Ta-incorporation concentration in double perovskites could be ascribed to the increasing band gaps, as has been verified in Figure 3. In addition, defect compensation, e.g., oxygen vacancies and Ta_{Bi} antisite defects, has been considered to be responsible for the low charge carrier concentration, which leads to low conductivity.[17,18] The computational results from Hautier and coworkers suggested the Bi-rich/Ta-poor condition is favorable for a higher carrier concentration,[18] which could be highly correlated to the declining PEC photocurrents as increasing the Ta concentration in the material.

EIS measurements were conducted, and the results are displayed in Figure 6. The Nyquist plots show a semicircle from high to medium frequencies for thin film photoelectrodes $Ba_2Bi_{1.6}Ta_{0.4}O_6$ and $Ba_2Bi_{1.5}Ta_{0.5}O_6$, followed by a second arc at low frequencies. In contrast, a huge semicircle can be observed over the entire experimental frequency range from 100 kHz to 0.1 Hz for the thin film photoelectrode $Ba_2Bi_{1.4}Ta_{0.6}O_6$. The equivalent circuit which fits and simulates the experimental EIS date is composed of a series resistance, R_s,[50,51] in series with two Randles circuits (RC). The first arc at high frequencies in the Nyquist plots are from the semiconductor photoelectrodes, represented by the semiconductor surface space charge capacitance, C_{sc}, as indicated in the equivalent circuit model and the semiconductor bulk resistance, R_{sc}, whose magnitude can be estimated from the radius of the arc in the Nyquist plot.[50] The second arc at low frequencies is associated with the electrolyte double layer capacitance, C_{dl}, and the charge transfer resistance, R_{ct}, at the semiconductor/electrolyte interface.[51] The simulated parame-

https://doi.org/10.1021/acs.jpcc.4c01309
J. Phys. Chem. C 2024, 128, 13177−13189

ters of the equivalent circuit elements are given in Table 1. From the photoelectrode $Ba_2Bi_{1.6}Ta_{0.4}O_6$ to the photoelectrode $Ba_2Bi_{1.4}Ta_{0.6}O_6$, the R_{sc} magnitudes increase sharply, manifesting a significant reduction in the bulk conductivity of the photoelectrodes. The R_{ct} values also exhibit an increasing trend, indicating that electron transport at the interface is inhibited when increasing the Ta-doping concentration. These results are consistent with the deteriorating collected photocurrents when increasing the Ta doping content from $x = 0.4$ to $x = 0.6$.

Mott−Schottky (M−S) measurements were carried out in a neutral electrolyte in the dark and are shown in Figure S5. The M−S plots exhibit a linear region and show negative slopes, which are consistent with the p-type semiconductivity. The M−S equation is a measure of the total interfacial capacitance $C_{interface}$ against the applied potentials. The $C_{interface}$ is a combination of the SCR capacitance C_{sc} in the semiconductor photoelectrode and the spatial capacitance C_{dl} from the electrolyte phase, $\frac{1}{C_{interface}} = \frac{1}{C_{sc}} + \frac{1}{C_{dl}}$ in an ideal surface-state-free situation.[44] Further in detail, C_{dl} is normally not a constant, as it is composed of the Helmholtz compact layer and a diffuse layer of charges in the solution. Thus, the expression of this double layer C_{dl} can further be written as a combination of two components in series, the Helmholtz compact layer capacitance C_H and the diffuse layer capacitance C_d, $\frac{1}{C_{dl}} = \frac{1}{C_H} + \frac{1}{C_d}$, according to the Gouy−Chapman−Stern (GCS) model. The C_H is independent of applied potential, whereas the C_d could change in a V-shaped manner as a function of potential with the theoretical minimum value near the potential of zero charge (PZC).[39] The total C_{dl} in the electrolyte phase is governed by the smaller capacitance and is often in the order of 10^{-5} F cm^{-2}.[44,52] The effect of C_{dl} induced potential drop can only be neglected and assume $C_{interface} \approx C_{sc}$ if $C_{dl} \gg C_{sc}$, preferably a capacitance difference of 2−3 orders of magnitude.[44,50] According to the extracted values of C_{dl} and C_{sc} in Table 1, the orders of C_{dl} are close to those of C_{sc} and thus should be taken into account. It is also noteworthy that in the case of very high dielectric constant and heavily doped semiconductors, e.g., ionized donor or acceptor concentrations on the scale of 10^{18}−10^{20} cm^{-3}, the inequality $C_{dl} \gg C_{sc}$ does not hold and a correction of the general M−S equation is needed.[53,54] As a result, the applied potential induced interface potential drop has contributions both from the semiconductor SCR and from the electrolyte double layer.[44,53,54] The M−S equation can be expressed as[53]

$$\frac{1}{C_{sc}^2} = \frac{2}{\varepsilon_r \varepsilon_0 e N_a}\left(E - E_{fb} - \frac{K_B T}{e}\right) + \frac{1}{C_{dl}^2} \quad (1)$$

where ε_0 is the vacuum permittivity, ε_r is the relative dielectric constant, e is the electronic charge, N_a is the acceptor concentration, E_{fb} is the flat band potential, K_B is the Boltzmann constant, and T is the absolute temperature. A linear relation between $\frac{1}{C_{sc}^2}$ and the applied potential is the typical sign to derive the semiconductor E_{fb}. The thermal term at room temperature K_BT has a small value of 0.0259 eV and can be corrected as desired.[12] The E_{fb} is derived from the intersection potential value with the abscissa axis in the linear region, E_{incept}.[55] Linear fitting extrapolation results in Figure S5 reveal that the E_{incept} values for $Ba_2Bi_{1.6}Ta_{0.4}O_6$ and $Ba_2Bi_{1.5}Ta_{0.5}O_6$ are 0.2 V_{RHE} and 0.02 V_{RHE}, respectively, corresponding to the E_{fb} of 0.17 V_{RHE} and −0.01 V_{RHE} after the thermal term correction and the solution drop correction. The mathematical expressions of E_v, N_a, and the effective density of states in the valence band N_V are included in eqs S9−S11. The calculated N_a for $Ba_2Bi_{1.6}Ta_{0.4}O_6$ and $Ba_2Bi_{1.5}Ta_{0.5}O_6$ are 2.44−6.28 × 10^{17} cm^{-3} and 3.39−8.74 × 10^{16} cm^{-3}, respectively. Our M−S experimental results are in line with previous theoretical investigations of the hole-killing defect compensation effects in BBTO-based double perovskite[17,18] and provide indirect evidence for defect compensation. Such defects, including oxygen vacancies and Ta_{Bi} antisites donor defects, compensate the p-type majority carriers and lead to low charge carrier densities in the material, which can be mitigated by increasing the Bi concentration in the compound.[18,56] This is demonstrated by the higher carrier concentration and larger photocurrent acquisition in the $Ba_2Bi_{1.6}Ta_{0.4}O_6$ photoelectrode than in the $Ba_2Bi_{1.5}Ta_{0.5}O_6$ photoelectrode. A resulting estimation of $N_V \approx 7.6 \times 10^{18}$ cm^{-3} is obtained. The derived E_V position for $Ba_2Bi_{1.6}Ta_{0.4}O_6$ spans a range of 0.24−0.26 V_{RHE} and the E_C is at around −1.52 ∼ −1.50 V_{RHE} based on the obtained experimental optical band gap of 1.76 eV. Similarly, calculations suggest that the E_V is at around 0.11−0.13 V_{RHE} and the E_C is at −1.81 ∼ −1.79 V_{RHE} for the $Ba_2Bi_{1.5}Ta_{0.5}O_6$ sample (Figure S5). These resulting energy band diagrams are very similar to the previously reported diagrams for pentavalent Nb^{5+} doped derivatives of BBO double perovskite,[12] where the HER potential is lower than the energy of the CB level, which is in favor of electron transfer toward the electrolyte phase. In the meantime, extra attention should be paid to the validity of the obtained E_{fb}. One of the most important fundamental assumptions behind the M−S equation is that the band edges of the semiconductor electrodes are fixed, and the E_F can shift its position under the influences from applied potentials or the potential unalignment with the electrolyte redox levels.[44] Earlier experiments on the electrochemical behaviors of undoped BBO and $Ba_2Bi_{1.8}Ta_{0.2}O_6$ double perovskites in Figure S3 showed pronounced reduction reactions of Bi^{3+} from 0.2 V_{RHE} to lower potentials. The coincidence that the obtained E_{fb} values of $Ba_2Bi_{1.6}Ta_{0.4}O_6$ and $Ba_2Bi_{1.5}Ta_{0.5}O_6$ samples fall in the vicinity of this reduction potential range makes it necessary to consider the nonidealities affecting the E_{fb} potentials. As has been discussed in the work of Fan and Bard,[55] contributions from the faradaic processes at the semiconductor/electrolyte interface could distort the M−S plot. When substantial e^- inject into the surface states of the semiconductors, the E_V edge would shift negatively and results in an E_{fb} shift to more negative potentials with the interference from interfacial Faradaic reactions. In the case of $Ba_2Bi_{1.6}Ta_{0.4}O_6$ and $Ba_2Bi_{1.5}Ta_{0.5}O_6$ photoelectrodes, reverse biasing photoelectrodes in the potential range negative of the OCP values could control the band bending and maintain the SCR to be depleted for the M−S investigation. In the meantime, it can also shift the band edges and E_{fb} to more negative values within the investigation potential ranges, which explains the potential difference from the OCP measurements and the photocurrent onset potential. This study systematically investigated the photoelectrode electronic band structures and electrochemical and PEC behaviors of the semiconductor/electrolyte interface by modulating the doping concentration in $Ba_2Bi_{2-x}Ta_xO_6$ ($0.2 \le x \le 0.8$) double perovskites. The direct experimental observation of the highly reversible polarizable photocurrents in this system could arouse intensive interests in optoelectronic

https://doi.org/10.1021/acs.jpcc.4c01309
J. Phys. Chem. C 2024, 128, 13177−13189

fields not limited to PEC solar water splitting, but also in optoelectronics such as switchable-logic gate applications,[23,57] p-channel thin film transistors, and hole transporting layers for photovoltaics.[11]

4. CONCLUSIONS

Double perovskites $Ba_2Bi_{2-x}Ta_xO_6$ ($0.2 \leq x \leq 0.8$) series are synthesized by a solution-assisted method. XRD results confirm the formation of a double perovskite structure. The systematic shift of characteristic peaks to higher angles indicates the successful incorporation of increasing Ta^{5+} contents in the BBO crystal lattice. The optical absorption spectra and Tauc plots reveal a trend of increasing optical band gaps for $Ba_2Bi_{2-x}Ta_xO_6$ ($0.2 \leq x \leq 0.8$) from 1.5 to 2.3 eV. Photoelectrochemical and electrochemical tests show that incorporation of Ta^{5+} is beneficial for improving the photoelectrode resistance to electrochemical corrosions. Both the cathodic photocurrents and the anodic photocurrents can be enhanced by the anodic poling treatment and the cathodic poling treatment, respectively. $Ba_2Bi_{1.6}Ta_{0.4}O_6$ exhibits both the highest cathodic photocurrent of 65.5 μA cm^{-2} at 0 V_{RHE} with an onset potential of 1.43 V_{RHE}, and the highest anodic photocurrent of 37 μA cm^{-2} at 2 V_{RHE} with an onset potential of 1.03 V_{RHE} among other Ta concentration samples. The deteriorating PEC photocurrents of Ta^{5+} concentration samples higher than the $Ba_2Bi_{1.6}Ta_{0.4}O_6$ photoelectrode are the result of both inferior light absorption ability due to large band gaps and lower charge carrier concentrations due to defect compensation.

■ ASSOCIATED CONTENT

Supporting Information

The Supporting Information is available free of charge at https://pubs.acs.org/doi/10.1021/acs.jpcc.4c01309.

Table for calculated tolerance factors and octahedral factors, magnified SEM images, digital images of $Ba_2Bi_{2-x}Ta_xO_6$ ($0.2 \leq x \leq 0.8$) double perovskite photoelectrodes, optical absorption and the corresponding Tauc-plot of the undoped parental BBO photoelectrode, LSV scan of the $Ba_2Bi_{1.8}Ta_{0.2}O_6$ photoelectrode under periodical on−off illumination, CV scans of an undoped BBO photoelectrode, changes in E_F of h^+ in a p-type semiconductor photoelectrode versus a RE, LSV curves of $Ba_2Bi_{1.4}Ta_{0.6}O_6$ photoelectrodes under cathodic scans and under anodic scans with intermittent 1 sun illumination, M−S plots of the $Ba_2Bi_{1.6}Ta_{0.4}O_6$ photoelectrode and the $Ba_2Bi_{1.5}Ta_{0.5}O_6$ photoelectrode in the dark, and the corresponding calculated energy band diagrams (PDF)

■ AUTHOR INFORMATION

Corresponding Author

Huub J. M. de Groot − *Leiden Institute of Chemistry, Leiden University, 2300 RA Leiden, The Netherlands;* orcid.org/0000-0002-8796-1212; Email: groot_h@chem.leidenuniv.nl

Authors

Tirong Guo − *Leiden Institute of Chemistry, Leiden University, 2300 RA Leiden, The Netherlands*

Wen Tian Fu − *Leiden Institute of Chemistry, Leiden University, 2300 RA Leiden, The Netherlands*

Complete contact information is available at: https://pubs.acs.org/10.1021/acs.jpcc.4c01309

Author Contributions

T.G. designed and conducted the experiments, performed data analysis and discussion, funding acquisition and wrote the first manuscript. W.T.F. contributed to idea conceiving for the strategies of material engineering, data discussion, crystal structure analysis and project supervision. H.J.M.de G. contributed to idea conceiving, data analysis and discussion, and project supervision. All authors discussed and revised the manuscript, and have given approval to the final version of the manuscript.

Notes

The authors declare no competing financial interest.

■ ACKNOWLEDGMENTS

We acknowledge the financial support from the China Scholarship Council (No. 201906250079).

■ REFERENCES

(1) Wang, W.; Xu, M.; Xu, X.; Zhou, W.; Shao, Z. Perovskite Oxide Based Electrodes for High-Performance Photoelectrochemical Water Splitting. *Angew. Chem., Int. Ed.* **2020**, *59*, 136−152.

(2) Tang, J.; Zou, Z.; Ye, J. Efficient Photocatalysis on $BaBiO_3$ Driven by Visible Light. *J. Phys. Chem. C* **2007**, *111*, 12779−12785.

(3) Hatakeyama, T.; Takeda, S.; Ishikawa, F.; Ohmura, A.; Nakayama, A.; Yamada, Y.; Matsushita, A.; Yea, J. Photocatalytic Activities of Ba_2RBiO_6 (R = La, Ce, Nd, Sm, Eu, Gd, Dy) under Visible Light Irradiation. *J. Ceram. Soc. Jpn.* **2010**, *118*, 91−95.

(4) Shtarev, D. S.; Shtareva, A. V.; Kevorkyants, R.; Molokeev, M. S.; Serpone, N. Revisiting the $BaBiO_3$ Semiconductor Photocatalyst: Synthesis, Characterization, Electronic Structure, and Photocatalytic Activity. *Photochem. Photobiol. Sci.* **2021**, *20*, 1147−1160.

(5) Sun, Q.; Wang, J.; Yin, W. J.; Yan, Y. Bandgap Engineering of Stable Lead-Free Oxide Double Perovskites for Photovoltaics. *Adv. Mater.* **2018**, *30* (15), 1705901.

(6) Matsushita, A.; Nakane, T.; Naka, T.; Isago, H.; Yamada, Y.; Yamada, Y. Valence States of Rare-Earth Ions and Band Gaps in $RBiBa_2O_6$ (R = La, Ce, Pr, Nd, Sm, Gd, Eu, and Dy) Photocatalysts. *Jpn. J. Appl. Phys.* **2012**, *51*, 121802.

(7) Yin, W.-J.; Weng, B.; Ge, J.; Sun, Q.; Li, Z.; Yan, Y. Oxide Perovskites, Double Perovskites and Derivatives for Electrocatalysis, Photocatalysis, and Photovoltaics. *Energy Environ. Sci.* **2019**, *12*, 442−462.

(8) Weng, B.; Xiao, Z.; Meng, W.; Grice, C. R.; Poudel, T.; Deng, X.; Yan, Y. Bandgap Engineering of Barium Bismuth Niobate Double Perovskite for Photoelectrochemical Water Oxidation. *Adv. Energy Mater.* **2017**, *7* (9), 1602260.

(9) Drost, R. J.; Fu, W. T. Preparation and Characterization of the Perovskites $BaCe_{1-x}Bi_xO_3$. *Mater. Res. Bull.* **1995**, *30*, 471−478.

(10) Mattheiss, L. F.; Hamann, D. R. Electronic Structure of the High-Tc Superconductor $Ba_{1-x}K_xBiO_3$. *Phys. Rev. Lett.* **1988**, *60*, 2681−2684.

(11) Shi, J.; Rubinstein, E. A.; Li, W.; Zhang, J.; Yang, Y.; Lee, T. L.; Qin, C.; Yan, P.; MacManus-Driscoll, J. L.; Scanlon, D. O.; Zhang, K. H. L.; et al. Modulation of the Bi^{3+} $6s^2$ Lone Pair State in Perovskites for High-Mobility p-Type Oxide Semiconductors. *Adv. Sci.* **2022**, *9* (6), 2104141.

(12) Ge, J.; Yin, W.-J.; Yan, Y. Solution-Processed Nb-Substituted $BaBiO_3$ Double Perovskite Thin Films for Photoelectrochemical Water Reduction. *Chem. Mater.* **2018**, *30*, 1017−1031.

(13) Chen, Z.; Jaramillo, T. F.; Deutsch, T. G.; Kleiman-Shwarsctein, A.; Forman, A. J.; Gaillard, N.; Garland, R.; Takanabe, K.; Heske, C.; Sunkara, M.; et al. Accelerating Materials Development for Photoelectrochemical Hydrogen Production: Standards for

Methods, Definitions, and Reporting Protocols. *J. Mater. Res.* **2010**, *25*, 3−16.
(14) Guo, T.; Fu, W. T.; de Groot, H. J. M. Engineering $Ba_2Bi_2O_6$ Double Perovskite with La^{3+} for High Current Density Visible Light Photoelectrochemical Hydrogen Evolution. *Small* **2024**, *20* (28), 2308781.
(15) Ma, J.; Guo, X.; Xue, H.; Pan, K.; Liu, C.; Pang, H. Niobium/Tantalum-based Materials: Synthesis and Applications in Electrochemical Energy Storage. *Chem. Eng. J.* **2020**, *380*, 122428.
(16) Shannon, R. D. Revised Effective Ionic Radii and Systematic Studies of Interatomic Distances in Halides and Chalcogenides. *Acta Crystallogr. A* **1976**, *32*, 751−767.
(17) Bhatia, A.; Hautier, G.; Nilgianskul, T.; Miglio, A.; Sun, J.; Kim, H. J.; Kim, K. H.; Chen, S.; Rignanese, G.-M.; Gonze, X.; et al. High-Mobility Bismuth-based Transparent p-Type Oxide from High-Throughput Material Screening. *Chem. Mater.* **2016**, *28*, 30−34.
(18) Dahliah, D.; Rignanese, G.-M.; Hautier, G. Defect Compensation in the p-type Transparent Oxide Ba_2BiTaO_6. *J. Mater. Chem. C* **2020**, *8*, 9352−9357.
(19) Gerischer, H. Neglected Problems in the pH Dependence of the Flatband Potential of Semiconducting Oxides and Semiconductors Covered with Oxide Layers. *Electrochim. Acta* **1989**, *34*, 1005−1009.
(20) Deng, J.; Han, F.; Schwarz, B.; Knapp, M.; Ehrenberg, H.; Hua, W.; Hinterstein, M.; Li, G.; He, Y.; Wang, J.; et al. Dielectric Relaxation and Magnetic Structure of A-Site-Ordered Perovskite Oxide Semiconductor $CaCu_3Fe_2Ta_2O_{12}$. *Inorg. Chem.* **2021**, *60*, 6999−7007.
(21) Panda, N.; Parida, B. N.; Padhee, R.; Choudhary, R. N. P. Dielectric and Electrical Properties of the Double Perovskite $PbBaBiNbO_6$. *J. Electron. Mater.* **2015**, *44*, 4275−4282.
(22) Zhou, Q.; Kennedy, B. J. High Temperature Structural Studies of Ba_2BiTaO_6. *Solid State Sci.* **2005**, *7*, 287−291.
(23) Cheng, Y.; Ye, J.; Lai, L.; Fang, S.; Guo, D. Ambipolarity Regulation of Deep-UV Photocurrent by Controlling Crystalline Phases in Ga_2O_3 Nanostructure for Switchable Logic Applications. *Adv. Electron. Mater.* **2023**, *9* (4), 2201216.
(24) Tian, Y.; Wang, A.; Wei, Y.; Pei, M.; Cao, R.; Gu, Z.; Yuan, Q.; Hu, Y.; Wang, J.; Liu, K.; Shang, D.; et al. Large-Area Printing of Ferroelectric Surface and Super-Domain for Solar Water Splitting. *Adv. Funct. Mater.* **2022**, *32* (19), 2111180.
(25) Bhuiyan, M. S.; Paranthaman, M.; Salama, K. Solution-Derived Textured Oxide Thin Films - a Review. *Supercond. Sci. Technol.* **2006**, *19*, R1−R21.
(26) Horvat-Radošević, V.; Kvastek, K. Role of Pt-Probe Pseudo-Reference Electrode in Impedance Measurements of Pt and Polyaniline (PANI) Modified Pt Electrodes. *J. Electroanal. Chem.* **2006**, *591*, 217−222.
(27) Wallwork, K. S.; Kennedy, B. J.; Zhou, Q.; Lee, Y.; Vogt, T. Pressure and Temperature-Dependent Structural Studies of Ba_2BiTaO_6. *J. Solid State Chem.* **2005**, *178*, 207−211.
(28) Xu, F.; Zhao, W.; Hu, X.; Weng, B. Sulfur Tuning Oxygen Vacancy of $Ba_2Bi_{1.4}Ta_{0.6}O_6$ for Boosted Photocatalytic Tetracycline Hydrochloride Degradation and Hydrogen Evolution. *J. Colloid Interface Sci.* **2023**, *636*, 470−479.
(29) Rodrigues, J. E. F. S.; Paschoal, C. W. D. A.; Silva, E. N.; Mince, K. A.; Lufaso, M. W. Relaxations in Ba_2BiTaO_6 Ceramics Investigated by Impedance and Electric Modulus Spectroscopies. *Mater. Res. Bull.* **2012**, *47*, 878−882.
(30) Mandal, P.; Sundaresan, A. Dielectric and Impedance Studies on the Double Perovskite Ba_2BiTaO_6. *Solid State Sci.* **2009**, *11*, 861−864.
(31) Li, C.; Lu, X.; Ding, W.; Feng, L.; Gao, Y.; Guo, Z. Formability of ABX_3 (X = F, Cl, Br, I) Halide Perovskites. *Acta Crystallogr.B* **2008**, *64*, 702−707.
(32) Khalfin, S.; Bekenstein, Y. Advances in Lead-Free Double Perovskite Nanocrystals, Engineering Band-Gaps and Enhancing Stability through Composition Tunability. *Nanoscale* **2019**, *11*, 8665−8679.
(33) Dolabella, S.; Borzi, A.; Dommann, A.; Neels, A. Lattice Strain and Defects Analysis in Nanostructured Semiconductor Materials and Devices by High-Resolution X-Ray Diffraction: Theoretical and Practical Aspects. *Small Methods* **2022**, *6* (2), 2100932.
(34) Holzwarth, U.; Gibson, N. The Scherrer Equation versus the'Debye-Scherrer Equation'. *Nat. Nanotechnol.* **2011**, *6*, 534.
(35) Harrison, W. T. A.; Reis, K. P.; Jacobson, A. J.; Schneemeyer, L. F.; Waszczak, J. S. Syntheses, Structures, and Magnetism of Barium/Rare-Earth/Bismuth Double Perovskites. Crystal Structures of Ba2MBiO6 (M = Ce, Pr, Nd, Tb, Yb) by Powder Neutron Diffraction. *Chem. Mater.* **1995**, *7* (11), 2161−2167.
(36) Mattheiss, L. F.; Hamann, D. R. Electronic Structure of $BaPb_{1-x}Bi_xO_3$. *Phys. Rev. B* **1983**, *28*, 4227−4241.
(37) Bratsch, S. G. Standard Electrode-Potentials and Temperature Coefficients in Water at 298.15 K. *J. Phys. Chem. Ref. Data* **1989**, *18*, 1−21.
(38) Vivier, V.; Regis, A.; Sagon, G.; Nedelec, J. Y.; Yu, L. T.; Cachet-Vivier, C. Cyclic Voltammetry Study of Bismuth Oxide Bi_2O_3 Powder by Means of a Cavity Microelectrode Coupled with Raman Microspectrometry. *Electrochim. Acta* **2001**, *46*, 907−914.
(39) Bard, A. J.; Faulkner, L. R. *Electrochemical Methods - Fundamentals and Applications*; John Wiley & Sons: New York, 2001.
(40) Berglund, S. P.; Abdi, F. F.; Bogdanoff, P.; Chemseddine, A.; Friedrich, D.; van de Krol, R. Comprehensive Evaluation of $CuBi_2O_4$ as a Photocathode Material for Photoelectrochemical Water Splitting. *Chem. Mater.* **2016**, *28*, 4231−4242.
(41) Bisquert, J.; Cendula, P.; Bertoluzzi, L.; Gimenez, S. Energy Diagram of Semiconductor/Electrolyte Junctions. *J. Phys. Chem. Lett.* **2014**, *5*, 205−207.
(42) Sato, N. *Electrochemistry at Metal and Semiconductor Electrodes*; Elsevier Science: Amsterdam, 1998.
(43) Deutsch, T. G.; Koval, C. A.; Turner, J. A. III-V Nitride Epilayers for Photoelectrochemical Water Splitting: GaPN and GaAsPN. *J. Phys. Chem. B* **2006**, *110*, 25297−25307.
(44) Hankin, A.; Bedoya-Lora, F. E.; Alexander, J. C.; Regoutz, A.; Kelsall, G. H. Flat Band Potential Determination: Avoiding the Pitfalls. *J. Mater. Chem. A* **2019**, *7*, 26162−26176.
(45) Bisquert, J. *Nanostructured Energy Devices - Equilibrium Concepts and Kinetics*; CRC Press: Boca Raton, 2014.
(46) Wang, Y.; Liu, J.; Huang, Y.; Wang, Z.; Li, Q.; Yue, S.; Liu, K.; Yan, S.; Liu, M.; Cao, D.; et al. Insights on the Origination of Ambipolar Photocurrent of Ferroelectric and the Improvement of Photoanodic Current. *J. Electrochem. Soc.* **2019**, *166*, H418−H424.
(47) Li, S.; AlOtaibi, B.; Huang, W.; Mi, Z.; Serpone, N.; Nechache, R.; Rosei, F. Epitaxial Bi_2 $FeCrO_6$ Multiferroic Thin Film as a New Visible Light Absorbing Photocathode Material. *Small* **2015**, *11*, 4018−4026.
(48) Gu, J.; Yan, Y.; Krizan, J. W.; Gibson, Q. D.; Detweiler, Z. M.; Cava, R. J.; Bocarsly, A. B. P-type $CuRhO_2$ as a Self-Healing Photoelectrode for Water Reduction under Visible Light. *J. Am. Chem. Soc.* **2014**, *136*, 830−833.
(49) Schroder, D. K.; Thomas, R. N.; Vine, J.; Nathanson, H. C. The Semiconductor Field-Emission Photocathode. *IEEE Trans. Electron Devices* **1974**, *21*, 785−798.
(50) Lopes, T.; Andrade, L.; Le Formal, F.; Gratzel, M.; Sivula, K.; Mendes, A. Hematite Photoelectrodes for Water Splitting: Evaluation of the Role of Film Thickness by Impedance Spectroscopy. *Phys. Chem. Chem. Phys.* **2014**, *16*, 16515−16523.
(51) Weng, B.; Grice, C. R.; Ge, J.; Poudel, T.; Deng, X.; Yan, Y. Barium Bismuth Niobate Double Perovskite/Tungsten Oxide Nanosheet Photoanode for High-Performance Photoelectrochemical Water Splitting. *Adv. Energy Mater.* **2018**, *8* (10), 1701655.
(52) Uosaki, K.; Kita, H. Effects of the Helmholtz Layer Capacitance on the Potential Distribution at Semiconductor/Electrolyte Interface and the Linearity of the Mott-Schottky Plot. *J. Electrochem. Soc.* **1983**, *130*, 895−897.
(53) Cardon, F.; Gomes, W. P. On the Determination of the Flat-Band Potential of a Semiconductor in Contact with a Metal or an

https://doi.org/10.1021/acs.jpcc.4c01309
J. Phys. Chem. C 2024, 128, 13177−13189

Electrolyte from the Mott-Schottky Plot. *J. Phys. D: appl. Phys.* **1978**, *11*, L63−L67.
(54) De Gryse, R.; Gomes, W. P.; Cardon, F.; Vennik, J. On the Interpretation of Mott-Schottky Plots Determined at Semiconductor/Electrolyte Systems. *J. Electrochem. Soc.* **1975**, *122*, 711−712.
(55) Fan, F.-R. F.; Bard, A. J. Semiconductor Electrodes: XXXVI. Characteristics of, Electrodes in Aqueous Solution. *J. Electrochem. Soc.* **1981**, *128*, 945−952.
(56) Yin, Y.; Wu, Y.; Chen, G.; Yin, W.-J. Double Perovskite Ba_2BiTaO_6 as a Promising p-Type Transparent Conductive Oxide: A First-Principles Defect Study. *J. Appl. Phys.* **2020**, *127*, 175703.
(57) Bouree, W. S.; Prevot, M. S.; Jeanbourquin, X. A.; Guijarro, N.; Johnson, M.; Formal, F. L.; Sivula, K. Robust Hierarchically Structured Biphasic Ambipolar Oxide Photoelectrodes for Light-Driven Chemical Regulation and Switchable Logic Applications. *Adv. Mater.* **2016**, *28*, 9308−9312.

https://doi.org/10.1021/acs.jpcc.4c01309
J. Phys. Chem. C 2024, 128, 13177−13189